

A Multiple-Regime Approach to Atmospheric Zonal-Flow Vacillation

by

Seongjoon Koo

Andrew W. Robertson

and

Michael Ghil

Department of Atmospheric Sciences and
Institute of Geophysics and Planetary Physics
University of California, Los Angeles
Los Angeles, CA 90095-1565

January 12, 2001

J. Atmos. Sci., 2nd revision

Corresponding author's address:

Seongjoon Koo

Department of Atmospheric Sciences

University of California, Los Angeles

Los Angeles, CA 90095-1565

E-mail: koo@atmos.ucla.edu

Phone: (310) 825-3439

Fax: (310) 206-5219

Abstract

Zonal-flow vacillation in an idealized two-layer, global, primitive-equation model is studied in the context of multiple regimes. The spatial structure of vertically and zonally averaged zonal-flow variability resembles that observed in the Southern Hemisphere, with dipolar anomalies centered at 40° and 60° .

The probability density function (PDF) of the model's zonal flow is studied in the subspace of its two leading principal components. The PDF exhibits a pronounced central peak with two distinct shoulders attached to it. All three features are statistically significant at the 95% confidence level against a red-noise null hypothesis and are argued to be the signature of multiple flow regimes. Flow composites for the two shoulders show meteorologically significant differences from climatology and similarities with observed Southern Hemisphere flow patterns. In the low-latitude regime the narrow jet's maximum lies equatorward of the climatological mean position, while in the high-latitude regime the broad jet is sometimes bimodal and has its maximum poleward of the climatological position. The residence times in the high- and low-latitude regimes are typically about 3 times as long as in the central-peak regime.

Both regimes' onsets are found to be abrupt, but the regime breaks exhibit a significant asymmetry: the low-latitude regime decays more slowly, while the high-latitude regime breaks rather abruptly. Eddy momentum forcing acts to maintain the zonal-flow regimes against surface drag. The changes in low-level eddy heat flux precede those of the eddy momentum forcing that drive both the regime onset and break. This phase difference between heat and momentum fluxes suggest that baroclinic processes play an important role in the regime transitions. The dependence of the preferred regimes' zonal-jet latitudes on bottom friction shows that multiple regimes coexist in a wide range of the parameter values.

1 Introduction

The zonally averaged zonal flow in the Southern Hemisphere (SH) exhibits pronounced low-frequency variability (LFV) on intraseasonal (Webster and Keller 1975) and interannual (Trenberth 1979) time scales. The dominant mode of the observed variability (Kidson 1988; Hartmann and Lo 1998) exhibits an equivalent barotropic vertical structure with dipolar anomalies centered near 40°S and 60°S. Recent observations (Hartmann and Lo 1998) indicate that there are no significant spectral peaks associated with this mode, although the mean duration of the extreme phases is estimated as 6.2 to 8.6 days. We shall use the term *zonal-flow vacillation* to indicate the irregular and aperiodic variations of the SH zonal jet.

Zonal-flow vacillation between two persistent anomalous states with irregular transitions between them suggests the concept of multiple regimes that originated in the work of Charney and DeVore (1979). The extent to which the LFV of planetary-scale atmospheric motion is well described by a small set of multiple regimes with abrupt transitions among them has been hotly debated. There is growing evidence, however, that observed atmospheric LFV in both the Northern Hemisphere (NH) and SH can be well described in these terms (Hansen and Sutera 1986; Mo and Ghil 1987, 1988; Mechoso et al. 1991; Cheng and Wallace 1993; Kimoto and Ghil 1993a, b; Michelangeli et al. 1995; Smyth et al. 1999).

Several attempts have been made to identify multiple regimes and bimodality associated with SH zonal-flow vacillation. Based on visual inspection of the zonal jet's position, Yoden et al. (1987) found two distinct flow regimes during the 1980–1983 austral winters, corresponding to single- and double-jet states. Akahori and Yoden (1997) studied the relationship between zonal-flow vacillation and wave breaking patterns of baroclinic eddies using an idealized model. They found bimodality in a histogram plot of an empirical measure of the typical latitude of wave breaking associated with the zonal-flow vacillation, the so-called LC index. However, no bimodality was found in a histogram of the zonal-mean flow's first

principal component (PC-1). Hartmann and Lo (1998) also reported finding no bimodality in PC-1 of the zonal-mean SH flow.

The main characteristics of zonal-flow vacillation and the dynamics of its two extreme phases are now relatively well understood. Modeling studies by Robinson (1991) and Yu and Hartmann (1993) and an observational study by Hartmann and Lo (1998) strongly suggest that both of the vacillation's extreme phases are maintained by the organized feedback between the zonal flow and the transient eddies.

High-frequency, synoptic-scale eddies with a period of less than 10 days play a key role in this feedback (Robinson 1991; Yu and Hartmann 1993). An observational study by Feldstein and Lee (1998) also found evidence of the feedback between the zonal flow and high-frequency eddies, although the feedback was less clear when the eddies were not filtered (Lee and Feldstein 1996; Feldstein and Lee 1996). Using an idealized model, Robinson (1996) demonstrated that the feedback depends upon the strength of bottom friction, and is prominent only for sufficiently strong surface friction. Robinson (2000) proposed a simple baroclinic mechanism based on quasi-geostrophic dynamics to explain this feedback.

Despite the advances in our understanding of the extreme phases described above, the dynamics of the *transition* phases of the vacillation remains poorly understood. For example, the origin of the initial eddy forcing that drives the zonal flow into one of the extreme phases is not clear. Nor is it known what causes these two relatively persistent phases of the vacillation to break.

In the present study we examine the probability density function (PDF) of the zonal flow in the simplified setting of an idealized atmospheric model of the type used by Hendon and Hartmann (1985). Our aim is to clarify the issue of multiple regimes, and to improve our understanding of the underlying dynamics. We demonstrate that the statistics of the vacillation's two extreme phases is consistent with the paradigm of multiple flow regimes. The time evolution of the vacillation is then traced in phase space as well as in physical space.

Composites with respect to onset and break of the two extreme phases of the vacillation can thus be constructed in a natural fashion.

Previous observational studies (Kidson 1988; Hartmann and Lo 1998) suggest that the vacillating zonal jet in the SH is mainly an eddy-driven mid-latitude phenomenon. This allows us to capture the fundamental dynamics of the zonal-flow vacillation using a relatively simple model, with no asymmetries in its lower boundary. Our simple model can easily be integrated for the long time spans required to obtain reliable statistics of the regimes and their entire evolution, from onset to break.

This paper is organized as follows: the numerical model is described in Section 2 and the multiple regimes of its zonal-mean flow are discussed in Section 3. In Section 4, we examine the time evolution of the vacillating zonal jet, with emphasis on the onset and break of the vacillation’s two extreme phases. The role of surface friction is investigated in Section 5 using additional sensitivity runs. A summary and discussion of the main results are provided in Section 6.

2 Model

The model used in this study is based on the atmospheric component of Saravanan and McWilliams’ (1995) coupled model and is very similar to the two-layer model of Hendon and Hartmann (1985). It is a dry primitive-equation model on a sphere. The governing equations in pressure coordinates are

$$\frac{\partial \zeta}{\partial t} = -\nabla \cdot (\zeta + f)\mathbf{V} - \mathbf{k} \cdot \nabla \times \left(\omega \frac{\partial \mathbf{V}}{\partial p} - \mathbf{F} \right), \quad (1)$$

$$\frac{\partial D}{\partial t} = \mathbf{k} \cdot \nabla \times (\zeta + f)\mathbf{V} - \nabla \cdot \left(\omega \frac{\partial \mathbf{V}}{\partial p} - \mathbf{F} \right) - \nabla^2 \left(\frac{\mathbf{V} \cdot \mathbf{V}}{2} + \Phi \right), \quad (2)$$

$$\frac{\partial \theta}{\partial t} = -\nabla \cdot (\theta \mathbf{V}) - \frac{\partial}{\partial p}(\theta \omega) + Q, \quad (3)$$

$$\nabla \cdot \mathbf{V} + \frac{\partial \omega}{\partial p} = 0, \quad (4)$$

$$\frac{\partial \Phi}{\partial p} = -\frac{R\theta}{p} \left(\frac{p}{p_0} \right)^{\frac{R}{c_p}}; \quad (5)$$

here \mathbf{k} denotes the vertical unit vector, ∇ the horizontal gradient operator, $\mathbf{V} \equiv (u, v)$ the horizontal velocity, $\zeta = \mathbf{k} \cdot \nabla \times \mathbf{V}$ the vertical component of relative vorticity, $D = \nabla \cdot \mathbf{V}$ the horizontal divergence, $\Phi \equiv gz$ the geopotential, ω the vertical velocity in pressure coordinates, θ the potential temperature, p_0 the surface pressure at 1000 hPa, \mathbf{F} the mechanical forcing, and Q the thermal forcing.

The above equations are discretized in the vertical following Lorenz (1960): the two layers have the same thickness, $\Delta p = 500$ hPa, and are centered at 250 hPa and 750 hPa. Due to the homogeneous lower boundary, boundary conditions are simply $\omega = 0$ at $p = 0$ and 1000 hPa. Even though the two-level configuration is a crude representation of the atmosphere, it has been used extensively and its properties are well documented. Hendon and Hartmann (1985) and Keppenne et al. (2000), in particular, reported that a two-level global primitive-equation model can produce realistic low-frequency behavior. Simple two-layer models have also been proven useful in theoretical studies of zonal-flow vacillation (Robinson 1991, 1996; Lee and Feldstein 1996) and in the study of advanced data assimilation methods (Ghil and Todling 1996).

For horizontal discretization, we adopt triangular truncation at T21. This relatively low resolution has been shown to capture the essential features of zonal-flow vacillation (Yu and Hartmann 1993) and is consistent with the simple 2-level discretization in the vertical. Comparable horizontal resolutions have been adopted in other previous studies of the problem

at hand (Robinson 1991, 1996; Lee and Feldstein 1996).

A T21 resolution results in a discrete model with 484 degrees of freedom. This number is much higher than that for low-order models, typically with $O(10)$ or fewer degrees of freedom, whose multiple equilibria have been shown to disappear when increasing the resolution (Cehelsky and Tung 1987). In fact, our model has a horizontal resolution that is much higher than Cehelsky and Tung’s (1987) 6×6 modes, which result in 78 degrees of freedom. Our model’s $O(10^2)$ degrees of freedom are comparable in number to various estimates of the large-scale atmosphere’s attractor dimension (Ghil and Childress 1987, pp. 193–195; Lions et al. 1997). The model’s time step is equal to 1 hour and results are saved every 24 hours.

The mechanical and thermal forcing terms within each model layer are chosen as follows:

$$\mathbf{F}_i = \gamma(\nabla^2 + \frac{2}{a^2})^4 \mathbf{V}_i - \frac{\delta_{i,2}}{\tau_E} \mathbf{V}_i, \quad (6)$$

$$Q_i = \gamma(\nabla^2)^4 \theta_i - \eta(\theta_i - \theta_{e,i}); \quad (7)$$

$i = 1, 2$ denote the upper and lower model levels, at 250 hPa and 750 hPa, respectively and $\delta_{i,j}$ represents the Kronecker delta. The scale-selective damping coefficient γ is chosen to act with a time scale of 1/4 day on the highest wavenumber resolved at our T21 truncation (Saravanan and McWilliams 1995). The Earth’s radius is $a = 6.4 \times 10^6$ m and the Ekman drag time scale τ_E is set to be 3 days. The radiative relaxation coefficient η is 15^{-1} days $^{-1}$. The radiative equilibrium potential temperature θ_e is prescribed to simulate perpetual-winter conditions, as in Hendon and Hartmann (1985).

The model with the parameter values described above was run for 30000 days and the first 300 days are discarded to avoid any initial transients. This model run is described and analyzed in Sections 3 and 4, while additional runs are studied in Section 5.

3 Multiple regimes in zonal-mean flow

a. PDF estimation

We apply a nonparametric density-estimation technique to search for multiple regimes in the latitudinal position of the model’s jet. A multivariate kernel density estimator (Silverman 1986) is used to estimate the PDF of the zonally and vertically averaged zonal-wind profile from the time series of 29700 daily profiles. This method was previously used by Kimoto and Ghil (1993a, b) to identify multiple flow regimes in the NH observed winter-time circulation.

First, a 10-day low-pass filter is applied to the time series of the zonally and vertically averaged zonal wind. The 31-point nonrecursive digital filter employs Lanczos smoothing to avoid Gibbs phenomena. Empirical orthogonal function (EOF) analysis was then performed on the low-pass filtered data by diagonalizing the covariance matrix. The filtering has little effect on the resulting EOF structures, although the fraction of variance described by the leading EOF increases slightly.

Figure 1 shows the two leading EOFs, which account for 62.1% and 17.2% of total variance, respectively. EOF-1 exhibits dipolar variability with maxima of opposite signs centered near 40° and 60° . Its node is located at 48° , which corresponds to the position of the model’s climatological zonal jet maximum. Thus, EOF-1 represents the zonal jet’s meridional displacement from its climatological mean position. The spatial structure of EOF-1 resembles its observed SH counterpart quite closely (Kidson 1988; Hartmann and Lo 1998), in spite of our model’s high degree of idealization. The second EOF exhibits an extremum near 50° , and is thus primarily associated with a strengthening and weakening of the climatological zonal jet.

[Figure 1 near here, please]

Before discussing details of PDF estimation, we first consider data scatter in phase space and its implications for PDF estimation. Data scatter in terms of “signal” and “noise” is

illustrated in Fig. 2 following Kimoto and Ghil (1993a). In Figs. 2a and 2b, the abscissa denotes the signal component defined by

$$\|\mathbf{x}\|_S \equiv \left(\sum_{i=1}^s c_i^2 \right)^{1/2}, \quad (8)$$

and the ordinate indicates the noise component defined by

$$\|\mathbf{x}\|_N \equiv \left(\sum_{i=s+1}^{10} c_i^2 \right)^{1/2}, \quad (9)$$

where c_i is the i -th PC; $s = 1$ in Fig. 2a and $s = 2$ in Fig. 2b. The diagonal line indicates a signal-to-noise ratio of 1. Here we have chosen to truncate the “noise” at 10 leading EOFs. These ten EOFs capture 99.99% of our model’s variance and the results in Fig. 2 are found, therefore, to be insensitive to increases in this number.

[Figure 2 near here, please]

If we take EOF-1 as the sole physical signal of zonal-mean flow variability, the majority of the data points fall into the upper triangle of Fig. 2a, where the signal-to-noise ratio is less than 1, and most of them are very close to the origin of the PC-1 axis. On the other hand, if we retain the two leading EOFs as the physical signal, as shown in Fig. 2b, the signal-to-noise ratio is substantially enhanced. Furthermore, many data points which previously lay near the climatological mean state are now away from the origin.

This result implies that if a PDF or histogram is computed using only PC-1, as in Akahori and Yoden (1997) or Hartmann and Lo (1998), a large fraction of the data points will fall near the origin, and any bimodality that might be present in the data could be obscured by noise [see also discussion in Mo and Ghil (1988) for NH regimes]. In order to avoid this situation, we proceed with PDF estimation in a two-dimensional (2-D) subspace spanned by the two leading EOFs. Including PC-3 in the “signal” does not change the data scatter in Fig. 2b substantially (not shown), so that we only retain the two leading EOFs.

As in Kimoto and Ghil (1993a) and Smyth et al. (1999), the PDF is estimated for a 2-D dataset that consists of the coefficients obtained by projecting the *unfiltered* zonally and

vertically averaged zonal wind anomalies onto the low-pass filtered EOFs shown in Fig. 1. This produces time series whose length equals that of the original dataset of 29700 daily profiles. Projecting the unfiltered data onto its own EOFs was found to yield a similar PDF but with a larger number of transient events.

An adaptive version of the kernel method that uses the Epanechnikov kernel (Kimoto and Ghil 1993a) is applied and Euclidean distance is employed as a similarity measure. The adaptive method uses a variable smoothing parameter according to the value of the estimated PDF at each sample point. This adaptive approach allows us to achieve more reliable estimates in the data-sparse regions that lie on the outskirts of the PDF (Silverman 1986).

The smoothing parameter h , which controls the smoothness of final density estimates, needs to be properly specified in order to avoid spurious peaks in the PDF. An objective way to determine this parameter is least-squares cross validation (LSCV), which minimizes an estimate of the integrated square error of the PDF fit (Silverman 1986). The LSCV scores are plotted as a function of the smoothing parameter h in Fig. 3. As is often the case in LSCV, the score has a fairly broad minimum, near $h = 0.3$ and 0.4 . Both values result in similar estimates of the PDF.

[Figure 3 near here, please]

The PDF constructed with $h = 0.4$ is displayed in Fig. 4a. The estimated PDF exhibits a pronounced central peak with two distinct shoulders attached to it. It is elongated along the PC-1 axis and has an overall crescent shape, with the two extremities dropping towards the negative PC-2 axis. Since EOF-2 describes a modulation in the strength of the climatological jet, this shape of the PDF is consistent with the climatological jet being weaker (negative PC-2) when the jet displacement (given by PC-1) is largest, and vice versa.

[Figure 4 near here, please]

In order to establish the statistical significance of the PDF's three distinct features—one

peak with two shoulders—we construct the null hypothesis to be a unimodal PDF with a non-Gaussian crescent shape which matches that in Fig. 4a. We describe in the Appendix a nonlinear stochastic model that generates random time series of 2-vectors that have such a PDF. One hundred sets of random time series were generated from this model, each with the same length as the original time series. A sample PDF is then computed from each of these 100 time series, using the same kernel method with the same smoothing parameter $h = 0.4$ as in Fig. 4a. These 100 sample PDFs have the non-Gaussian shape of the original PDF and often exhibit multimodality by chance, due to the random nature of the time series from which they are computed.

The percentage of random PDFs so generated that fall short of the PDF values shown in Fig. 4a is plotted in Fig. 4b, with regions containing values that exceed 95% shaded. Both the peak and the shoulders in Fig. 4a are significant at the 95% confidence level. Although the PDF in Fig. 4a does not show three distinct peaks, the significance test indicates that there are three highly populated regions in phase space. Each of these three regions contains one of the regime centroids and deviates significantly from the unimodal crescent-shaped PDF. Regions of high significance also occur near the two tips of the crescent-shaped PDF, where the stochastic model—in spite of its high level of sophistication—does not capture the original PDF well [cf. Fig. 4a and Fig. A1(b)].

Probability density estimation, a major concern of this study, is solely based on the *recurrence* of particular flow patterns so that it does not, in principle, distinguish physically meaningful, quasi-steady, low-frequency phenomena from transient noise. As a result, transient noise that recurs frequently can also have high probability density and this may obscure inherent multiple regimes that might be present in the data. In order to examine this possibility, we consider a subset of the original data that represents quasi-stationary (QS) states.

First, the speed along the phase-space trajectory is computed for each day, using Eu-

clidean distance between the two vectors two days apart in the 2-D phase plane shown in Fig. 4. A centered difference scheme is used to compute the speed. We then select only QS days, whose speed lies below a prescribed value, taken to be the time mean minus one standard deviation. The resulting QS dataset consists of 4642 days. Note that the method described above is more conservative than Mo and Ghil’s (1987, 1988) use of pattern correlations to define slow change in the field of interest for a number of successive days, as shown by Vautard et al. (1988).

Figure 5 shows the PDF estimated for this QS subset, with the smoothing parameter $h = 0.4$ that was determined by the LSCV. Its general shape resembles Fig. 4a, but it exhibits three distinct PDF peaks, whose locations are very close to the peak and two shoulders in the PDF of the full dataset. This strongly suggests that the two shoulders are the trace of two distinct PDF peaks that exist inherently in the full dataset, but are obscured by transient noise.

[Figure 5 near here, please]

In order to corroborate further the evidence for the multiple regimes, we apply Gaussian mixture model clustering (Smyth et al. 1999) to the 2-D dataset used in the kernel density estimation. In this method, a PDF is assumed to be a linear combination of a few Gaussian component density functions, each with its own mean and covariance. Thus, a PDF can be multimodal in this more general sense, even if it exhibits only one distinct peak (Titterton et al. 1985). Unlike other clustering techniques, this method uses a consistent data-driven methodology based on cross-validated likelihood to estimate the number of clusters supported by the data.

First, we compute the cross-validated log-likelihood, following the procedures described in Smyth et al. (1999). Figure 6 shows the log-likelihood values against the number of clusters k . The likelihood curve exhibits a sharp increase from $k = 1$ and then begins to saturate as k is increased further. The minimum at $k = 1$ clearly indicates that a single Gaussian

is most unlikely to represent the data PDF. When we increase the maximum number of clusters from 6 to 10, the log-likelihood exhibits even more clearly the asymptotic nature of the saturation from $k = 3$ on (not shown). This behavior suggests that we are experiencing the “overfitting” of a non-Gaussian PDF by an ever larger number of Gaussian clusters. A histogram of PC-1 (not shown) exhibits indeed deviations from Gaussianity, characterized by a lower central peak and shorter tails.

[Figure 6 near here, please]

We choose therefore $k = 3$ as the optimal trade-off between goodness-of-fit and statistical stability of the clusters’ centroids and other parameters. Indeed, the log-likelihood curve starts to flatten out at this value, which agrees with the number of distinct peaks in Fig. 5.

Given the number of clusters $k = 3$, we fit a three-component mixture model to the 2-D dataset used in the kernel density estimations. Figure 7 shows the location of the means of the Gaussians and the standard-deviation ellipses associated with their covariance matrices. The three ellipses agree with the general shape of the PDFs estimated by the kernel method, with a crescent shape elongated along the PC-1 axis. Two of the ellipses are mainly located on the positive and negative side of the PC-1 axis, respectively. The other ellipse is centered close to the origin with a slight shift toward the positive PC-1 and PC-2 axes. The mixture model thus supports the results of the kernel density estimation.

[Figure 7 near here, please]

b. Physical characteristics of the regimes

We now construct regime composites in order to examine the physical-space picture associated with the three high-density regions in Figs. 4, 5 and 7. First, the location of the regime centroids in Fig. 4a is found by using the bump-hunting algorithm of Fukunaga and Hostetler (1975); the resulting centroids are denoted by ‘+’. These regime centroids in phase space are then converted to physical-space patterns, and pattern correlations between

the centroids' profiles and daily zonal-mean wind profiles are computed.

We then identify recurrent *episodes* into a given regime by collecting the days whose pattern correlation with the corresponding centroid is greater than 0.8. The results that are shown in this section and the next two are not sensitive to small changes in this threshold value. The approximate regime boundaries set by this criterion are non-overlapping and are indicated as V-shaped heavy lines in Fig. 4a. These lines represent only approximate boundaries because pattern correlation was computed in physical space, rather than the reduced 2-D phase subspace. The composite patterns so obtained are not sensitive to either choice. Pattern correlation is used to define regime membership in order to collect flow profiles with similar shapes, rather than similar amplitudes. This agrees with the usual meteorological intuition that a larger significance should be attached to an anomaly's spatial pattern rather than to its magnitude (Kimoto and Ghil 1993b).

Finally, regime *events* are defined by taking recurrent episodes whose duration is equal to or longer than 6 days. Thus, regime events incorporate, by definition, recurrent and persistent patterns of zonal-mean flow. Flow composites of the resulting regime events are shown in Fig. 8, revealing three distinct anomalous zonal-jet states. Almost identical profiles (not shown) are obtained when episodes shorter than 6 days are also included.

[Figure 8 near here, please]

In Regime 2, called hereafter the *low-latitude regime*, the jet is located equatorward of its climatological mean position, while in Regime 3, hereafter the *high-latitude regime*, it is located poleward of this position. Finally, in Regime 1, hereafter the *central regime*, the jet is strengthened near its climatological mean position. The low- and high-latitude regimes correspond to the shoulders near the positive and negative PC-1 axis in Fig. 4a, respectively. Thus, the composite anomalies of the two regimes reflect to a large extent the two opposite phases of EOF-1 in Fig. 1.

Although the regime composites in Fig. 8 might suggest a single zonal jet shifting merid-

ionally, careful inspection of the zonally and vertically averaged zonal flow on a daily basis reveals the occurrence of double jets during the high-latitude regime (not shown). These double jets are especially clear and more frequently observed at the upper level. Figure 9 shows the zonal-mean wind at each level composited with respect to the low- and high-latitude regime events.

[Figure 9 near here, please]

At the upper level, the high-latitude regime exhibits a broad profile with evidence of a double jet (Fig. 9b), while a single jet with strong meridional shear characterizes the low-latitude regime (Fig. 9a). Contrasts in vertical shear between the two regimes are also apparent in the figure. As evident from Fig. 9, the zonal-flow vacillation in our model is not characterized simply by the meridional displacement of a single jet, but by more complex changes in the meridional wind profile that are often associated (see also Fig. 11) with transitions between single- and double-jet states.

c. Statistical characteristics of the regimes

The regimes' persistence characteristics are summarized in Fig. 10 by plotting the number of recurrent episodes whose duration exceeds the number of days indicated on the abscissa. The three straight lines indicate least-square linear fits to the data scatter for the three regimes. The number of recurrent episodes declines, in all three regimes, according to an approximate power law, i.e. the points for each regime fall close to a straight line in the log-linear coordinates of Fig. 10. The situation for our zonally symmetric SH model regimes is thus similar to that recorded by Dole and Gordon (1983) and Kimoto and Ghil (1993b) for NH observations and by Legras and Ghil (1985) for their model's zonally asymmetric regimes.

[Figure 10 near here, please]

For a linear first-order Markov process with mean zero, the number of “runs” of a given

duration—i.e., of times that a prescribed sign persisted for that duration or longer—is given by a straight line in log-linear coordinates (Ghil and Childress 1987, pp. 181ff. and 323ff.). For example, consider the following linear first-order Markov process in continuous time:

$$\frac{du}{dt} = -\lambda u + \eta(t), \quad (10)$$

where $u = u(t)$, λ is constant, and η represents Gaussian white noise with mean zero. By taking the ensemble mean,

$$\frac{d\langle u \rangle}{dt} = -\lambda \langle u \rangle, \quad (11)$$

and the solution $\langle u \rangle = U(t)$ is given by

$$U(t) = u_o e^{-\lambda t}. \quad (12)$$

The ensemble mean $\langle u \rangle = U(t)$ converges to zero as $t \rightarrow \infty$ regardless of its initial state. The “drift” or (negative) feedback coefficient $-\lambda$ is the reciprocal of the process’s exponential relaxation time or e -folding time $\tau = 1/\lambda$. The value of λ can be estimated from the slope of the process’s persistence diagram when plotted in log-linear coordinates, as done in Fig. 10.

The e -folding times for the three regimes are thus estimated from the straight regression lines shown in Fig. 10, following Dole and Gordon (1983) for Northern Hemisphere observations and Legras and Ghil (1985) for a barotropic model with topography. For the central regime the estimate is $\tau = 3.1$ days, while the low- and high-latitude regimes have $\tau = 11.0$ and 12.8 days, respectively. Evidently, the central regime is about three times less persistent than the other two regimes. This short persistence time is mainly due to the volume occupied by the central regime being considerably smaller than that of the other two regimes (see Fig. 4a).

We investigate next the statistical properties of regime transitions, adopting a Markov-chain description (Ghil 1987; Mo and Ghil 1987, 1988; Vautard et al. 1990; Kimoto and Ghil 1993b). First, we construct the transition matrix \mathbf{T} , whose element T_{ij} gives the

number of transitions from regime i to j . The corresponding transition probability P_{ij} is estimated as $P_{ij} = T_{ij}/n_i$, where n_i is the total number of passages through regime i . The simulated dataset here is much longer than the observed datasets of the above-mentioned papers. This allows us to report actual transition probabilities P_{ij} as opposed to the previous reports of transition counts T_{ij} only.

Figure 11 shows the Markov chain of regime transitions, considering all regime episodes regardless of their durations. The two highest transition probabilities correspond to persistence of the low- or high-latitude regimes and these estimated probabilities are statistically significant at the 99% level, according to the test of Mo and Ghil (1988). The central regime shows low return probability, consistent with its relatively small area in phase subspace (Fig. 4a) and its proximity to the other two regimes.

[Figure 11 near here, please]

Only the direct transition from the central to the high-latitude regime has an estimated probability that is statistically significant at the 99% level. Nonetheless, direct transitions between the low- and high-latitude regimes have higher probabilities than those between the two extreme regimes via the central regime. For example, the direct transition from the high- to the low-latitude regime has a probability of 0.16, while the transition via the central regime shows a probability of only $0.12 \times 0.32 = 0.04$. The mean transition time for re-entry is similar for all three regimes, while that of transitions between different regimes shows the longest wandering between the low- and high-latitude regimes. Hereafter, we focus only on the two more persistent regimes that characterize the extreme phases of zonal-flow vacillation.

4 Time evolution of zonal-flow vacillation

a. Model diagnostics and compositing procedures

The essence of zonal-flow vacillation can be described in the quasi-geostrophic, zonally averaged equations on a β -plane:

$$\frac{\partial \bar{u}}{\partial t} = f_o \bar{v} - \frac{\partial}{\partial y}(\overline{u'v'}) + \bar{F}, \quad (13)$$

$$\frac{\partial \bar{\theta}}{\partial t} = -\bar{\omega} \frac{\partial \Theta}{\partial p} - \frac{\partial}{\partial y}(\overline{v'\theta'}) + \bar{Q}, \quad (14)$$

$$f_o \frac{\partial \bar{u}}{\partial p} = \hat{R} \frac{\partial \bar{\theta}}{\partial y}, \quad (15)$$

where an overbar denotes a zonal average and a prime indicates a deviation from the zonal average. The zonal-average mechanical forcing \bar{F} is dominated by surface friction [see Eq. (6)]; \bar{Q} is the zonal-average thermal forcing [Eq. (7)], $\Theta = \Theta(p)$ the reference potential temperature, and $\hat{R} = (p/p_o)^\kappa R/p$ the normalized gas constant.

For a given mechanical forcing \bar{F} , the zonal momentum Eq. (13) states that zonal wind is driven by the Coriolis acceleration due to meridional motion and by the meridional convergence of westerly eddy momentum flux. If Eq. (13) is vertically averaged using the upper and lower boundary conditions, the Coriolis acceleration term vanishes and the eddy momentum flux convergence becomes the only driving forcing of the zonal-flow vacillation against the frictional drag. For a given thermal forcing \bar{Q} , potential temperature is controlled by two competing terms in the thermodynamic Eq. (14): the adiabatic cooling/heating term associated with vertical motion and the eddy heat flux convergence/divergence term due to meridional temperature advection by eddies. The thermal-wind Eq. (15) links the dynamics governed by Eq. (13) and the thermodynamics controlled by Eq. (14). Equations (13)–(15) are now used to examine the dynamics of the low- and high-latitude regimes.

In order to investigate the time evolution of the model's zonal-flow vacillation, composites for the two extreme phases of the vacillation were constructed. First, days belonging to either a low- or high-latitude regime event are numbered consecutively, e.g. [1, 2, \dots , n], and then

normalized to constitute a closed time interval of $[0, 10]$. The choice of this standardized event duration of 10 days is motivated by the average durations of the low- and high-latitude regime events, which are 10.2 and 10.1 days, respectively. The days corresponding to the standardized times $t = 0$ and $t = 10$ days are defined to constitute the regime’s onset and break, respectively. The actual data points within the standardized time interval $[0, 10]$ are interpolated for each event to 11 equidistant points, using cubic spline interpolation. Note that the actual signals at regime onset and break are not affected by this interpolation.

We now collect days before the onset and after the break, selecting the same number of days before and after as the duration of the specific regime event itself. The same normalization and interpolation techniques are applied to these two time intervals on either side of the regime, resulting in the standardized time intervals of $[-10, 0]$ and $[10, 20]$. By combining these three intervals, we have the temporal evolution of a regime event for the normalized time interval $[-10, 20]$ with increments of 1.

The above procedures are repeated for all 277 and 289 events of the low- and high-latitude regimes, respectively. Composites of key physical variables are made for these events with respect to the standardized time interval of $[-10, 20]$. In the following subsection, we only show the interval $[-4, 14]$ for clarity. The method described above provides a very compact view of the entire evolution of the regimes, from onset to break, in a single figure. In contrast to the middle-day composites used by Feldstein and Lee (1996), our method does not smear out the signals associated with regime onset and break. We have verified that composites computed with respect to regime onset and break without the scaling described above (not shown) yield very similar results to those reported in the following.

b. Onset, maintenance, and break

Figure 12 shows anomaly composites of key variables with respect to the standardized regime evolution for the low- (left panels) and high-latitude (right panels) regimes. Shaded

regions are statistically significant at the 95% level by a two-sided pointwise t -test. Panels (a) and (b) show the vertically averaged zonal mean wind and clearly demonstrate the dipolar nature of the zonal-flow variability centered at 40° and 60° , consistent with Fig. 8b and previous SH observations. The low-latitude regime exhibits less variability within the regime itself than the high-latitude regime, resulting in a near steady state.

[Figure 12 near here, please]

In order to measure the rate of changes in the zonal-wind profile shown in Figs. 12a and 12b, we compute the root-mean-square (RMS) difference between two meridional profiles two days apart, using a centered difference scheme, and divide it by the time interval elapsed. The quantity so obtained is a measure of the acceleration (or deceleration) of the zonal mean wind, and equivalent to the speed along the model's phase-space trajectory [see Legras and Ghil (1985) for a NH model and Vautard (1990) for NH observations]. The composites of this acceleration with respect to standardized regime evolution are shown in Fig. 13.

[Figure 13 near here, please]

A similar picture (not shown) is obtained by compositing the phase-space trajectory's speed, in the 2-D phase plane spanned by the projection coefficients of the two leading EOFs shown in Fig. 1. This similarity bears out further the fact that the two leading principal components do indeed constitute the signal, as suggested by the results in Fig. 2.

During the regime maintenance phase, the low-latitude regime exhibits a lower RMS acceleration than the high-latitude regime. This is consistent with Figs. 12a and 12b, which show less variability within the low-latitude regime than the high-latitude regime.

Abrupt onsets are clearly observed for both the low- and high-latitude regimes. On the other hand, the regime break shows an interesting asymmetry: a slower change is observed for the low-latitude regime while an abrupt break is clear for the high-latitude regime.

The statistical significance of the asymmetry between the breaks of the low- and high-latitude regimes is tested in the following way. First, we collect the RMS zonal-wind ac-

celeration of the 277 low-latitude regime breaks and the 289 high-latitude regime breaks. The 566 samples are then randomly shuffled one hundred times. For each random shuffling, composites of 277 and 289 samples are computed, resulting in 100 sets of the sample means. Finally, the lower 5% and upper 95% values of these 100 sets are compared with the composites of the RMS accelerations associated with the low- and high-latitude regime breaks. The asymmetry between the breaks of the two regimes is found to be significant at the 95% level. Similarly, the asymmetry between the onset and the break of the low-latitude regime is also found to be significant at the 95% level.

Figures 12c and 12d depict the vertical shear of the zonal mean wind, which is closely related to the horizontal temperature gradient through the thermal-wind balance. The anomalies near 40° and 60° , which correspond to zones of anomalous baroclinicity, are roughly in phase with the anomalies in the vertically averaged zonal mean wind. Panels (e) and (f) of Fig. 12 show anomalies of vertically averaged eddy momentum flux convergence, i.e. the forcing of the zonal mean wind [see Eq. (13)]. The in-phase nature of the barotropic zonal mean wind anomalies and the eddy momentum flux convergence demonstrates that the eddy momentum forcing acts to maintain the anomalous position of the jet against surface friction, consistent with previous studies (Robinson 1991; Yu and Hartmann 1993; Hartmann and Lo 1998).

At the time of regime onset, anomalously strong eddy momentum forcing is observed for both regimes, consistent with the abrupt changes in zonal-mean flow observed in Fig. 13. Eddy momentum forcing near break exhibits an asymmetry between the low- and high-latitude regimes. In the case of the low-latitude regime, the eddy momentum forcing anomalies become very small near the break, consistent with the low RMS zonal-wind acceleration at the break shown in Fig. 13. The high-latitude regime break, on the other hand, is accompanied by a poleward shift of the negative eddy momentum forcing anomalies from the mid-latitudes. This feature is associated with the more rapid termination of the high-latitude

regime.

Panels (g) and (h) of Fig. 12 show the low-level eddy heat flux. Prior to regime onset, strong positive anomalies in the eddy heat flux are observed at the central latitudes of both regimes. They are followed by eddy momentum forcing anomalies (Figs. 12e and 12f) and thus by abrupt acceleration of zonal mean wind anomalies at the time of regime onset (Fig. 13). This demonstrates the baroclinic nature of the eddies that drive the zonal-mean wind anomalies. The temporal lag between the evolution of the eddy heat flux and the eddy momentum flux convergence, on the one hand, and the near-simultaneous occurrence of changes in the eddy momentum forcing and zonal wind acceleration, on the other, are consistent with the dynamical picture suggested by the studies discussed in Section 1. In this picture, equatorward propagation of baroclinic eddies and subsequent eddy mean-flow interactions lead to eddy momentum forcing that accelerates the upper-level zonal-mean flow.

As mentioned in Section 1, it is now recognized that the persistence of zonal wind anomalies during the extreme phases of the vacillation is due to the reinforcement of the anomalous zonal flow by the convergence of transient eddy momentum fluxes. In the context of the model regimes, the idealized feedback argument runs as follows: upon an initial eddy momentum forcing, the zonal-mean wind starts to accelerate near 40° and 60° for the low- and high-latitude regime, respectively. The stronger eddy momentum forcing at the upper level and the deceleration of the low-level flow by surface friction lead to differential acceleration in the vertical. The enhanced vertical shear feeds baroclinic instability that generates baroclinic eddies. The resulting eddies propagate preferentially equatorward due to the sphericity of the earth, and associated eddy zonal-mean flow interactions lead to an eddy momentum flux convergence at the upper level, closing the feedback loop.

The low-level eddy heat flux in Figs. 12g and 12h shows a distinct asymmetry between the low- and high-latitude regime. The low-latitude regime displays dipolar anomalies centered

at 40° and 60° . The positive eddy heat flux anomalies along 40° persist until standardized time $t = 7$ days, at which time they begin to attenuate (Fig. 12g); this is consistent with a similar behavior of the eddy momentum forcing at 40° (Fig. 12e). The high-latitude regime, on the other hand, shows very weak positive anomalies at 60° throughout the event, while strong negative anomalies dominate in mid-latitudes (Fig. 12h). These negative anomalies extend poleward, nearly up to 60° , and increase in magnitude until the regime break; this is consistent with the poleward shift in eddy momentum forcing near the high-latitude regime break (Fig. 12f). For both the low- and high-latitude regimes, the changes in the low-level eddy heat flux near the regime break (Figs. 12g and 12h) precede those of eddy momentum forcing (Figs. 12e and 12f) by one normalized day or so, as in the case for the regime onset.

5 Dependence on surface friction

Surface friction plays an important role in regime maintenance, balancing anomalous eddy momentum forcing [see Eq. (13)]. In order to examine further the influence of surface friction on zonal-flow vacillation, six additional runs were carried out, all having the same length of 30000 days as the control run. All parameter values were held fixed in the seven runs except for the Ekman drag time scale τ_E , which controls the strength of the frictional bottom drag [see Eq. (6)]. The seven values of τ_E were 1.0, 1.5, 2.0, 2.5, 3.0 (control), 4.0 and 8.0 days.

Bivariate PDFs of the zonally and vertically averaged zonal-wind profiles were constructed for each of the seven runs, as described in Section 3. The precise locations of the peaks and shoulders were obtained using the bump-hunting algorithm, in the subspace of the two leading EOFs. Depending on the parameter value τ_E , we identified one, two or three zonal-flow regimes. As in Section 3, data points that have pattern correlations of 0.8 or higher with the regime centroids in physical space were collected, and the corresponding composite profiles of zonally and vertically averaged zonal wind were computed.

The resulting latitudinal positions of the zonal-jet maxima are plotted relative to the

reciprocal Ekman drag time scale $1/\tau_E$ in Fig. 14. For an intermediate range of bottom-friction values of $1.5 \text{ days} \leq \tau_E \leq 4 \text{ days}$, multiple zonal-jet regimes coexist. The zonal jet's latitudinal position and its intensity jump irregularly from one regime to another within this range. For the smallest or largest values of surface drag, only one zonal-jet regime obtains. This is similar to Akahori and Yoden's (1997) result that the bimodality of their LC index depends on the surface drag.

[Figure 14 near here, please]

Surface friction is found to have a substantial impact on the zonal-mean flow. The run using the lowest drag (highest value of τ_E) exhibits stronger and more agitated flows than the control run; there is decreased power in the ultra low-frequency band (period $T > 60$ days) and increased power in the higher-frequency band of the zonal flow's power spectrum (not shown). Overall, lower drag values yield zonal jets that are displaced further poleward. Robinson (1997) showed that this poleward shift of the barotropic jet is due to the changes in the meridional structure of the eddy momentum fluxes that force it.

On the other hand, the highest-drag run shows weaker flows with reduced high-frequency variability and enhanced low-frequency variability of the zonal-mean flow. This is consistent with Robinson's (1996) result that the enhanced baroclinicity due to increased surface drag leads to more persistent zonal jets. These jets arise from the stronger feedback between the high-frequency eddies and the zonal-mean flow.

6 Concluding remarks

a. Multiple regimes and their key properties

In the present paper, we have investigated zonal-flow vacillation in a two-layer global primitive equation model. This vacillation is characterized by irregular meridional fluctuations of the zonal jet. In spite of its high degree of idealization, our model simulates well the

observed meridional structure of zonal-flow variability in the SH, with equivalent-barotropic anomalies of opposite signs centered at 40° and 60° .

Motivated by previous studies of multiple regimes, we have applied two advanced density estimation techniques, the kernel method and Gaussian mixtures, to model simulations of the zonally and vertically averaged zonal wind. In order to obtain results with high statistical significance, simulations that are 30000 days long were used. Using the kernel method, the PDF in the phase subspace spanned by the two leading EOFs of the zonal wind field is found to exhibit a pronounced central peak with two distinct “shoulders” attached to it (Fig. 4). All three of these features are statistically significant at the 95% confidence level against a null hypothesis of bivariate red noise.

Restricting the analysis to a quasi-stationary data subset of days when the phase-space trajectory has slower speeds yields three distinct PDF peaks (Fig. 5). The Gaussian mixture model clearly indicates that a single Gaussian process is extremely unlikely to have generated the PDF of the data. The mixture model also provides independent evidence for three underlying clusters (Figs. 6 and 7).

These PDF measures strongly suggest that the two-layer model’s zonal-flow vacillation is well described by the paradigm of multiple flow regimes. As discussed in Section 1, bimodality or multiple regimes in zonal-mean flow were found neither by Akahori and Yoden (1997) in a simple global circulation model nor by Hartmann and Lo (1998) in SH observations. This major difference between their results and ours appears to be due to the fact that our analysis was performed in a 2-D phase subspace using a kernel density estimator while previous studies relied on one-dimensional (1-D) histograms. The analysis of the signal-to-noise ratio in the model simulation (Fig. 2) demonstrates the necessity of signal description in the 2-D subspace spanned by the two leading EOFs. We have verified that a similar PDF estimation in a 1-D subspace using PC-1 only does not yield strong evidence of either bimodality or multiple regimes. These results are consistent with Mo and Ghil (1988), who

showed that inhomogeneity of a PDF, i.e. deviations from Gaussianity, can be detected more easily in a multi-dimensional space since the peaks and shoulders of the PDF are not necessarily located on the PC-1 axis, as shown in Fig. 4a (see also Kimoto and Ghil 1993a).

Flow composites associated with the regime centroids capture three distinct zonal-jet states. A strong jet near its climatological mean position is associated with the central peak in the PDF. The two PDF shoulders (or additional peaks, depending on the dataset and estimation method) have the jet maximum located equatorward (*low-latitude regime*) or poleward (*high-latitude regime*) of its climatological position. The high-latitude regime is found to be associated with a double jet at the upper level, while the low-latitude regime is characterized by a strong single jet with enhanced meridional shear (Figs. 8 and 9). This asymmetry in jet structure suggests that zonal-flow vacillation does not simply involve meridional shifts in the jet's position and changes in its intensity.

The strong asymmetry between the two off-climatology regimes suggests that zonal-flow vacillation is not a manifestation of linear oscillations about the climatological mean jet. This idea is supported by the Markov chain of regime transitions in Fig. 11. Indeed, direct transitions between the low-and high-latitude regimes, without passing through the central regime, have probabilities that are considerably higher than those for transitions that pass through the central regime. Furthermore, the typical persistence of the two extreme regimes is about three times as long as that of the near-climatology regime.

b. Standardized evolution of regime events

To investigate the temporal evolution of the vacillating zonal jet we restricted our attention to persistent regime events, lasting 6 days or longer. Consistent with previous studies, we found that baroclinic eddies act to maintain the zonal-flow regimes via weakening or strengthening of the poleward transfer of westerly momentum from lower latitudes. The high correlation between the zonal-wind anomalies and the eddy momentum forcing anoma-

lies suggests a substantial feedback between the two. The eddy momentum forcing at regime onset is preceded by anomalous low-level eddy heat flux, consistent with previous studies (Lee and Feldstein 1996; Feldstein and Lee 1996; Robinson 2000). Eddy heat flux changes lead those in eddy momentum flux convergence by about 1 or 2 normalized days, while changes in eddy momentum forcing and zonal wind acceleration occur simultaneously. These lead-lag relationships are consistent with a dynamical picture in which equatorward propagation of baroclinic eddies and subsequent eddy mean-flow interactions lead to eddy momentum forcing that accelerates the upper-level zonal-mean flow.

Both regimes' onsets are found to be abrupt (Fig. 13). The breaks, however, show a significant asymmetry between the two regimes: an abrupt break is evident for the high-latitude regime, while it is more gradual for the low-latitude regime. The eddy momentum flux convergence that forces the zonal-mean flow exhibits a similar asymmetry between the two regime breaks (Figs. 12e and 12f). The low-latitude regime break is accompanied by a collapse of the momentum flux convergence at the key latitude 40° (Fig. 12e), while the high-latitude regime break appears to be driven by the shift of negative forcing anomalies from 40° to 50° (Fig. 12f). Changes in the low-level eddy heat flux near regime break also precede those of the eddy momentum forcing, as in the case of the regime onset. Baroclinic processes appear thus to be important for both regime onset and regime break.

The asymmetry between the regime breaks is reminiscent of the early concept of a NH zonal-index cycle (Rossby and Willett 1948; Namias 1950). These authors described the index cycle as a relaxation oscillation, with slow transitions from low to high index and fast transitions from high to low index. Willett (1948) found that the low- and high-index phases of the NH jet are associated with latitudinal shifts of the jet as well as changes in its intensity. Thus, they would correspond, very roughly, to our low- and high-latitude regimes, respectively. Although the importance of the index cycle in the NH has been criticized (e.g. Wallace and Hsu 1985), there has been a recent resurgence of interest in the

zonally symmetric mode of variability in the NH (Thompson and Wallace 2000; Thompson et al. 2000). Wallace (2000) has drawn further attention to the connections between a zonally symmetric seesaw or “annular mode” [see also Mo and Ghil’s (1988) “North-South oscillation,” their Fig. 10d] and the North Atlantic Oscillation [see also the sectorial and hemispheric features of Keppenne et al.’s (2000) 70-day oscillation].

Depending on the strength of bottom friction, we found one, two or three zonal-flow regimes, with multiple regimes present for the Ekman drag time scale τ_E between 1.5 and 4.0 days (Fig. 14). In this parameter range, the time evolution of the zonal jet is characterized by irregular jumps from one regime to another. Model simulations that used higher drag values tend to exhibit reduced high-frequency variability of zonal jets. This is consistent with Robinson’s (1996) conclusion that the enhanced baroclinicity due to increased surface drag leads to more persistent zonal jets as the feedback between the high-frequency eddies and the zonal flow becomes stronger. Overall, lower-drag runs yield stronger zonal jets that are displaced further poleward.

The dependence of flow regime on bottom drag and the coexistence of multiple regimes in Fig. 14 is reminiscent of the *S*-shaped bifurcation curves that arise from back-to-back saddle-node bifurcations [e.g., Figs. 6.5 and 10.6 in Ghil and Childress (1987)]. The details of the bifurcations, if indeed present, remain to be worked out, along with the stability of the distinct branches that arise from them.

We have presented evidence of multiple regimes associated with opposite phases of zonal-flow vacillation in our idealized flat-bottom primitive-equation model. Clearly these regimes cannot be explained by the theories of multiple flow equilibria that emphasize the role of topography (Charney and DeVore 1979; Charney and Straus 1980; Benzi et al. 1986; Ghil and Childress 1987, Ch. 6). The question of the relevance of our regimes to the observed SH’s zonal-mean flow also remains to be answered. Further investigations, based on observational as well as on hierarchical modeling studies (Ghil and Robertson 2000), are required to resolve

the remaining questions raised in this discussion of our results.

Acknowledgments. We would like to thank Dr. R. Saravanan for providing his atmospheric model, which became the basis of the model used in this study. Fruitful discussions with Drs. M. Kimoto, K. Ide and S. Feldstein are gratefully acknowledged. The manuscript benefited substantially from careful reviews by W. Robinson and two anonymous reviewers. This research was supported by the University of California's Campus Laboratory Collaboration (CLC) program (SK), DOE Grant DE-FG03-98ER62615 (AWR) and NASA grant NAG 5-713 (MG). This is publication number 5387 of UCLA's Institute of Geophysics and Planetary Physics.

Appendix

A stochastic model to test statistical significance of the PDF

In Section 3a, we assess the statistical significance of the three distinct features of the PDF in Fig. 4a. The null hypothesis postulated is a unimodal PDF with the non-Gaussian crescent shape of the deterministic model simulation's PDF. In order to generate random time series of 2-vectors that have such a PDF, we construct a nonlinear stochastic model based on a 2-D Langevin equation (Kloeden and Platen 1992):

$$\begin{pmatrix} dx \\ dy \end{pmatrix} = -\beta \begin{pmatrix} \frac{\partial V}{\partial x} \\ \frac{\partial V}{\partial y} \end{pmatrix} dt + \epsilon^{1/2} \begin{pmatrix} dW_1 \\ dW_2 \end{pmatrix}. \quad (\text{A1})$$

Here V is a potential function that determines a mean drift (deterministic forcing) via its gradient, and $d\mathbf{W} = (dW_1, dW_2)$ is a 2-D Wiener process with two independent components. Each component of $d\mathbf{W}$ has zero mean and variance equal to dt . The two parameters β and ϵ determine the strength of the two competing terms on the right-hand side, that is, mean drift and diffusion.

We derive the potential function V from the deterministic model's simulated flow history such that the asymptotic solution of Eq. (A1) has a unimodal crescent-shaped PDF. To obtain such a form, we let

$$V = -\frac{\epsilon}{2} \log P^*, \quad (\text{A2})$$

where P^* is a very strongly smoothed PDF of the deterministic model data. This P^* is chosen so as to yield the unimodal distribution that is closest to the one in Fig. 4a, but before any sign of the multimodality appears in the distribution. The logarithmic functional form in Eq. (A2) is motivated by the solution of the Fokker-Planck equation corresponding to Eq. (A1). The same approach has been used by Hansen and Sutura (1995) in the context of a 1-D problem. Figure A1 (a) shows the resulting potential function.

[Figure A1 near here, please]

The two parameters β and ϵ in Eq. (A1) are chosen so as to generate a random time series of 200 000 samples whose PDF is as close as possible to the highly smoothed PDF P^* and whose decorrelation times are equal to those of the deterministic model's output. The random time series is obtained by numerically solving the stochastic differential equation (A1) using the Euler method (Kloeden and Platen 1992). The decorrelation times are defined by

$$T^{(x)} = \int_{-t_1}^{+t_1} \rho^{(x)}(t) dt, \quad (\text{A3})$$

$$T^{(y)} = \int_{-t_2}^{+t_2} \rho^{(y)}(t) dt, \quad (\text{A4})$$

where $\rho^{(x)}(t)$ and $\rho^{(y)}(t)$ are the autocorrelations of PC-1 and PC-2 time series at lag t , and t_1 and t_2 are approximate zero-crossing times, chosen to be 70 days and 35 days, respectively. The decorrelation times of the deterministic model output are $T^{(x)} = 44$ days and $T^{(y)} = 17$ days.

Under these constraints, the model parameter values are given by $\beta = 0.21$ and $\epsilon = 3.20$ with time step $\Delta t = 0.15$ days. Slight differences, less than 10%, in variance of simulated time series from that of the deterministic model output are adjusted before any PDF estimations, so that both the simulated and original time series have the same variance. Figure A1 (b) shows the asymptotic PDF estimated from the simulated time series of 200 000 samples by Eq. (A1). This estimated PDF is unimodal and has the general crescent shape of the PDF shown in Fig. 4a.

References

- Akahori, K. and S. Yoden, 1997: Zonal flow vacillation and bimodality of baroclinic eddy life cycles in a simple global circulation model. *J. Atmos. Sci.*, **54**, 2349–2361.
- Benzi, R., A. Speranza, and A. Sutera, 1986: A minimal baroclinic model for the statistical properties of low-frequency variability. *J. Atmos. Sci.*, **43**, 2962–2967.
- Cehelsky, P. and K. K. Tung, 1987: Theories of multiple equilibria and weather regimes—A critical reexamination. Part II: Baroclinic two-layer models. *J. Atmos. Sci.*, **44**, 3282–3303.
- Charney, J. G. and J. G. DeVore, 1979: Multiple flow equilibria in the atmosphere and blocking. *J. Atmos. Sci.*, **36**, 1205–1216.
- Charney, J. G. and D. M. Straus, 1980: Form-drag instability, multiple equilibria and propagating planetary waves in baroclinic, orographically forced, planetary wave systems. *J. Atmos. Sci.*, **37**, 1157–1176.
- Cheng, X. and J. M. Wallace, 1993: Cluster analysis of the Northern Hemisphere wintertime 500-hPa height field: Spatial patterns. *J. Atmos. Sci.*, **50**, 2674–2696.
- Dole, R. M. and N. D. Gordon, 1983: Persistent anomalies of the extratropical Northern Hemisphere wintertime circulation: Geographical distribution and regional persistent characteristics. *Mon. Wea. Rev.*, **111**, 1567–1586.
- Feldstein, S. and S. Lee, 1996: Mechanisms of zonal index variability in an aquaplanet GCM. *J. Atmos. Sci.*, **53**, 3541–3555.
- Feldstein, S. and S. Lee, 1998: Is the atmospheric zonal index driven by an eddy feedback? *J. Atmos. Sci.*, **55**, 3077–3086.
- Fukunaga, K. and L. D. Hostetler, 1975: The estimation of the gradient of a density function. *IEEE Trans. Info. Thy.*, **IT-21**, 32–40.

- Ghil, M., 1987: Dynamics, statistics, and predictability of planetary flow regimes. In C. Nicolis and G. Nicolis (Eds.), *Irreversible Phenomena and Dynamical Systems Analysis in the Geosciences*. D. Reidel, pp. 241–283.
- Ghil, M. and S. Childress, 1987: *Topics in Geophysical Fluid Dynamics: Atmospheric Dynamics, Dynamo Theory, and Climate Dynamics*. Springer-Verlag, 485 pp.
- Ghil, M. and A. W. Robertson, 2000: Solving problems with GCMs: General Circulation Models and their role in the climate modeling hierarchy. In D. Randall (Ed.), *General Circulation Model Development: Past, Present, and Future*. Academic Press, pp. 285–325.
- Ghil, M. and R. Todling, 1996: Tracking atmospheric instabilities with the Kalman filter. 2. Two-layer results. *Mon. Wea. Rev.*, **124**, 2340–2352.
- Hansen, A. R. and A. Sutera, 1986: On the probability density distribution of planetary-scale atmospheric wave amplitude. *J. Atmos. Sci.*, **43**, 3250–3265.
- Hansen, A. R. and A. Sutera, 1995: The role of topography in the low-frequency variability of the large-scale midlatitude circulation. *J. Atmos. Sci.*, **52**, 2497–2508.
- Hartmann, D. L. and F. Lo, 1998: Wave-driven zonal flow vacillation in the Southern Hemisphere. *J. Atmos. Sci.*, **55**, 1303–1315.
- Hendon, H. H. and D. L. Hartmann, 1985: Variability in a nonlinear model of the atmosphere with zonally symmetric forcing. *J. Atmos. Sci.*, **42**, 2783–2797.
- Keppenne, C. L., S. L. Marcus, M. Kimoto, and M. Ghil, 2000: Intraseasonal variability in a two-layer model and observations. *J. Atmos. Sci.*, **57**, 1010–1028.
- Kidson, J. W., 1988: Indices of the Southern Hemisphere zonal wind. *J. Climate*, **1**, 183–194.

- Kimoto, M. and M. Ghil, 1993a: Multiple flow regimes in the Northern Hemisphere winter. Part I: Methodology and hemispheric regimes. *J. Atmos. Sci.*, **50**, 2625–2643.
- Kimoto, M. and M. Ghil, 1993b: Multiple flow regimes in the Northern Hemisphere winter. Part II: Sectorial regimes and preferred transitions. *J. Atmos. Sci.*, **50**, 2645–2673.
- Kloeden, P. E. and E. Platen, 1992: *Numerical Solution of Stochastic Differential Equations*. Springer-Verlag, 632 pp.
- Lee, S. and S. Feldstein, 1996: Mechanism of zonal index evolution in a two-layer model. *J. Atmos. Sci.*, **53**, 2232–2246.
- Legras, B. and M. Ghil, 1985: Persistent anomalies, blocking and variations in atmospheric predictability. *J. Atmos. Sci.*, **42**, 433–471.
- Lions, J. L., O. P. Manley, R. Teman, and S. Wang, 1997: Physical interpretation of the attractor dimension for the primitive equations of atmospheric circulation. *J. Atmos. Sci.*, **54**, 1137–1143.
- Lorenz, E. N., 1960: Energy and numerical weather prediction. *Tellus*, **12**, 364–373.
- Mechoso, C., J. Farrara, and M. Ghil, 1991: Intraseasonal variability of the winter circulation in the Southern Hemisphere atmosphere. *J. Atmos. Sci.*, **48**, 1387–1404.
- Michelangeli, P.-A., R. Vautard, and B. Legras, 1995: Weather regimes: Recurrence and quasi stationarity. *J. Atmos. Sci.*, **52**, 1237–1256.
- Mo, K. C. and M. Ghil, 1987: Statistics and dynamics of persistent anomalies. *J. Atmos. Sci.*, **44**, 877–901.
- Mo, K. C. and M. Ghil, 1988: Cluster analysis of multiple planetary flow regimes. *J. Geophys. Res.*, **93**, 10927–10952.
- Namias, J., 1950: The index cycle and its role in the general circulation. *J. Meteor.*, **7**, 130–139.

- Robinson, W. A., 1991: The dynamics of the zonal index in a simple model of the atmosphere. *Tellus*, **43A**, 295–305.
- Robinson, W. A., 1996: Does eddy feedback sustain variability in the zonal index? *J. Atmos. Sci.*, **53**, 3556–3569.
- Robinson, W. A., 1997: Dissipation dependence of the jet latitude. *J. Climate*, **2**, 176–182.
- Robinson, W. A., 2000: A baroclinic mechanism for the eddy feedback on the zonal index. *J. Atmos. Sci.*, **57**, 415–422.
- Rossby, C.-G. and H. C. Willett, 1948: The circulation of the upper troposphere and lower stratosphere. *Science*, **108**, 643–652.
- Saravanan, R. and J. C. McWilliams, 1995: Multiple equilibria, natural variability, and climate transitions in an idealized ocean-atmosphere model. *J. Climate*, **8**, 2296–2323.
- Silverman, B. W., 1986: *Density Estimation for Statistics and Data Analysis*. Chapman and Hall, 175 pp.
- Smyth, P., K. Ide, and M. Ghil, 1999: Multiple regimes in Northern Hemisphere height fields via mixture model clustering. *J. Atmos. Sci.*, **56**, 3704–3723.
- Thompson, D. W. J. and J. M. Wallace, 2000: Annular modes in the extratropical circulation. Part I: Month-to-month variability. *J. Climate*, **13**, 1000–1016.
- Thompson, D. W. J., J. M. Wallace, and G. C. Hegerl, 2000: Annular modes in the extratropical circulation. Part II: Trends. *J. Climate*, **13**, 1018–1036.
- Titterton, D. M., A. F. M. Smith, and U. E. Makov, 1985: *Statistical Analysis of Finite Mixture Distributions*. John Wiley and Sons, 243 pp.
- Trenberth, K. E., 1979: Interannual variability of the 500-mb zonal mean flow in the Southern Hemisphere. *Mon. Wea. Rev.*, **107**, 1515–1524.

- Vautard, R., 1990: Multiple weather regimes over the North Atlantic: Analysis of precursors and successors. *Mon. Wea. Rev.*, **118**, 2056–2081.
- Vautard, R., B. Legras, and M. Déqué, 1988: On the source of midlatitude low-frequency variability. Part I: A statistical approach to persistence. *J. Atmos. Sci.*, **45**, 2811–2843.
- Vautard, R., K. C. Mo, and M. Ghil, 1990: Statistical significance test for transition matrices of atmospheric Markov chains. *J. Atmos. Sci.*, **47**, 1926–1931.
- Wallace, J. M., 2000: North Atlantic Oscillation/annular mode: Two paradigms—one phenomenon. *Quart. J. R. Met. Soc.*, **126**, 791–805.
- Wallace, J. M. and H. H. Hsu, 1985: Another look at the index cycle. *Tellus*, **37A**, 478–486.
- Webster, P. J. and J. L. Keller, 1975: Atmospheric variations: vacillations and index cycles. *J. Atmos. Sci.*, **32**, 1283–1300.
- Willett, H. C., 1948: Patterns of world weather changes. *Trans. Amer. Geophys. Union*, **29**, 803–809.
- Yoden, S., M. Shiotani, and I. Hirota, 1987: Multiple planetary flow regimes in the Southern Hemisphere. *J. Meteor. Soc. Japan*, **65**, 571–585.
- Yu, J.-Y. and D. L. Hartmann, 1993: Zonal flow vacillation and eddy forcing in a simple GCM of the atmosphere. *J. Atmos. Sci.*, **50**, 3244–3259.

List of Figures

1	The two leading EOFs of the 10-day low-pass filtered zonally and vertically averaged zonal flow.	40
2	Data scatter in terms of leading EOFs. (a) Abscissa is the root-mean square (RMS) magnitude of anomalies in phase space computed with only PC-1, and ordinate is the RMS magnitude of anomalies with PC-2 through PC-10. (b) Abscissa is the RMS magnitude of anomalies computed with PC-1 and PC-2, and ordinate is the RMS magnitude of anomalies with PC-3 through PC-10.	41
3	Least-squares cross validation (LSCV) scores as a function of the smoothing parameter h . The scores on the ordinate are only defined up to an arbitrary constant equal to the sum of squares of the true (but unknown) PDF [see Fig. 9 and Eqs. (A.1) and (A.2) in Kimoto and Ghil (1993a)].	42
4	Estimated PDF of the zonal-flow profile. (a) Two-dimensional PDF on a plane spanned by EOF-1 and EOF-2, with a smoothing parameter $h = 0.4$; axes are scaled by the standard deviation of PC-1 and contours are increasing from 0.04 (outermost) in intervals of 0.04. The symbol '+' denotes regime centroids and heavy lines indicate approximate regime boundaries (see text for details). (b) Number, out of 100, of random PDFs that fell short of the PDF values shown in (a). Contour interval is 10 and the regions with values larger than 95 are shaded.	43
5	Same as Fig. 4a but for the quasi-stationary dataset.	44
6	Cross-validated log-likelihood per sample as a function of the number of clusters, computed by randomly dividing the dataset into two equal partitions 20 times; see Smyth et al. (1999) for details.	45

7	Mixture model estimates of regime centroids, denoted by the symbol *, and covariance ellipses, superimposed on the data scatter. Only every 50th data point has been plotted for clarity.	46
8	Composites of zonally and vertically averaged (a) total and (b) anomalous zonal-wind profile that belongs to the regime events.	47
9	Composites of zonal mean wind at the two model levels for the (a) low- and (b) high-latitude regime events.	48
10	Persistence diagram of recurrent episodes.	49
11	Markov chain of regime transitions. Numbers indicate transition probability and mean transition time (in parenthesis). Transitions that are statistically significant (Mo and Ghil 1988) at the 99% level are drawn as heavy arrows.	50
12	Composite anomalies with respect to standardized regime evolution: (a) and (b) vertically averaged zonal mean wind; (c) and (d) vertical wind shear; (e) and (f) vertically averaged eddy momentum flux convergence; and (g) and (h) low-level eddy heat flux. The left panels are for the low-latitude regime and the right panels for the high-latitude regime. Regime onset and break correspond to nondimensionalized time 0 and 10, respectively. The contour interval in (a) and (b) is 1.0 ms^{-1} , in (c) and (d) is 0.5 ms^{-1} , in (e) and (f) is $2.5 \times 10^{-6} \text{ ms}^{-2}$, and in (g) and (h) is 0.5 Kms^{-1} . Solid contours are positive, dashed ones are negative, and zero contour is omitted. Shaded areas are statistically significant at the 95% level (see text for details).	51

13	Composites of a root-mean-square (RMS) measure of acceleration of zonal mean wind, with respect to standardized regime evolution. This measure of acceleration is defined by the RMS difference between two meridional profiles, two days apart, of zonally and vertically averaged zonal wind, divided by the time elapsed. Onset and break correspond to the normalized epochs of 0 and 10 days, respectively. Dashed lines indicate a 95% confidence interval for the estimated climatological mean value of the RMS acceleration.	52
14	Dependence of the latitudinal position of the preferred regimes' zonal-jet maximum on bottom friction.	53
A1	(a) Potential function used in Eq. (A1) to generate random time series. Contours are increasing from 3 (innermost one) in intervals of 3. (b) Asymptotic PDF of random time series of 200 000 samples generated from Eq. (A1) using the potential function in (a). Contours are increasing from 0.04 (outermost) in intervals of 0.04, as in Fig. 4a.	54

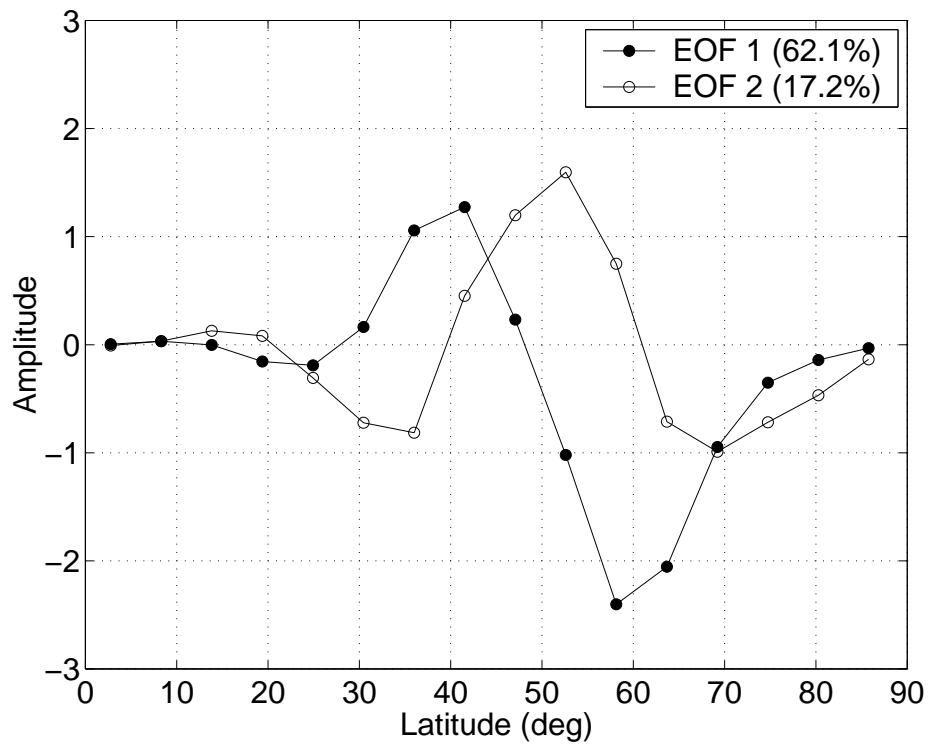


Figure 1: The two leading EOFs of the 10-day low-pass filtered zonally and vertically averaged zonal flow.

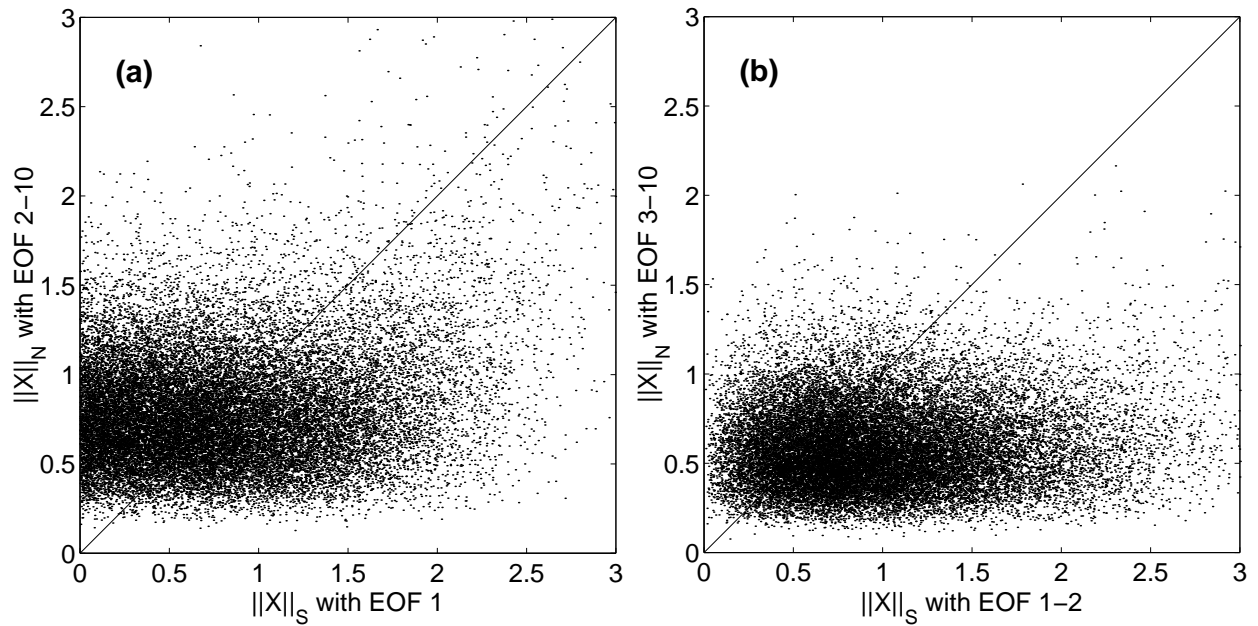


Figure 2: Data scatter in terms of leading EOFs. (a) Abscissa is the root-mean square (RMS) magnitude of anomalies in phase space computed with only PC-1, and ordinate is the RMS magnitude of anomalies with PC-2 through PC-10. (b) Abscissa is the RMS magnitude of anomalies computed with PC-1 and PC-2, and ordinate is the RMS magnitude of anomalies with PC-3 through PC-10.

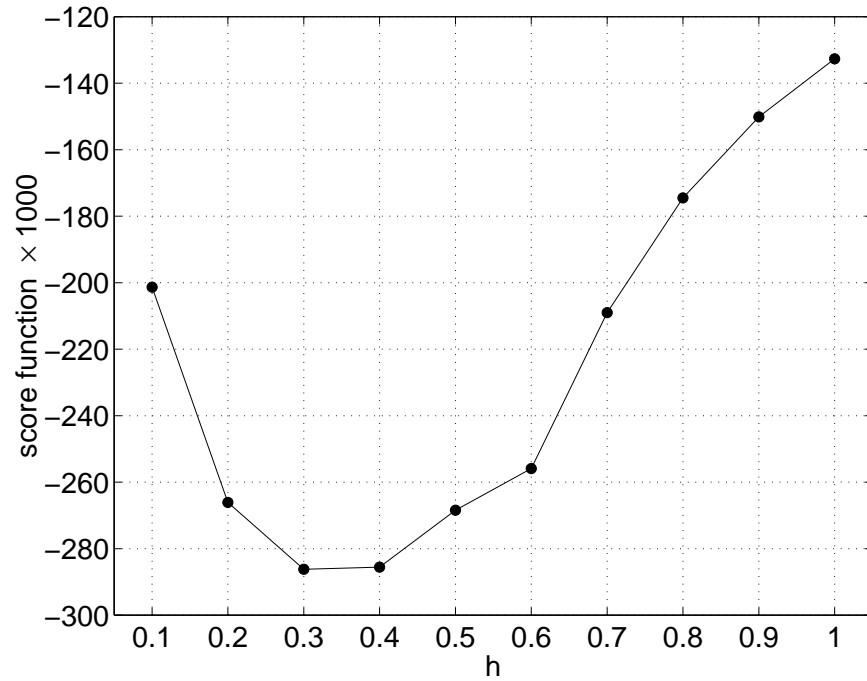


Figure 3: Least-squares cross validation (LSCV) scores as a function of the smoothing parameter h . The scores on the ordinate are only defined up to an arbitrary constant equal to the sum of squares of the true (but unknown) PDF [see Fig. 9 and Eqs. (A.1) and (A.2) in Kimoto and Ghil (1993a)].

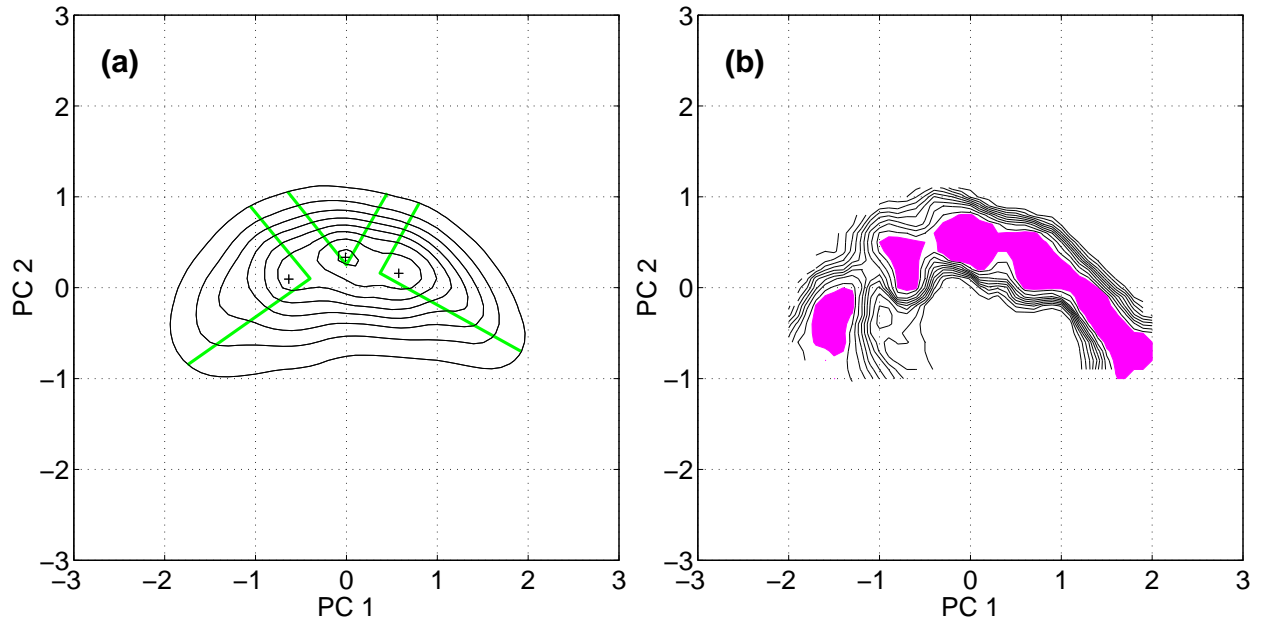


Figure 4: Estimated PDF of the zonal-flow profile. (a) Two-dimensional PDF on a plane spanned by EOF-1 and EOF-2, with a smoothing parameter $h = 0.4$; axes are scaled by the standard deviation of PC-1 and contours are increasing from 0.04 (outermost) in intervals of 0.04. The symbol '+' denotes regime centroids and heavy lines indicate approximate regime boundaries (see text for details). (b) Number, out of 100, of random PDFs that fell short of the PDF values shown in (a). Contour interval is 10 and the regions with values larger than 95 are shaded.

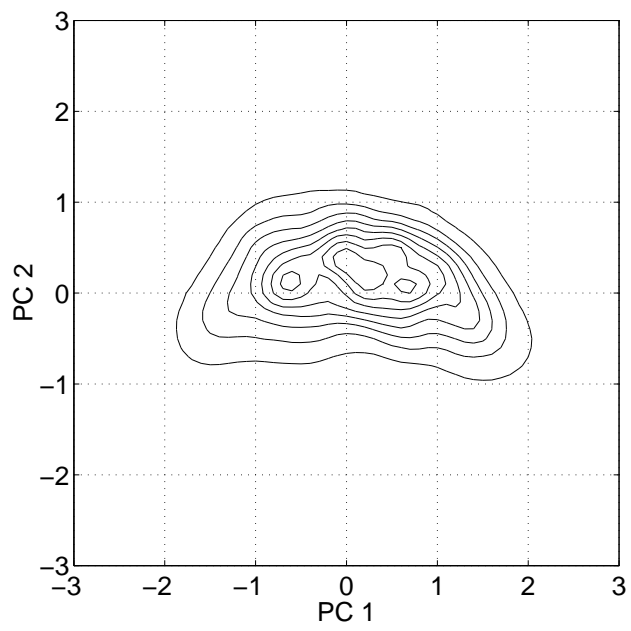


Figure 5: Same as Fig. 4a but for the quasi-stationary dataset.

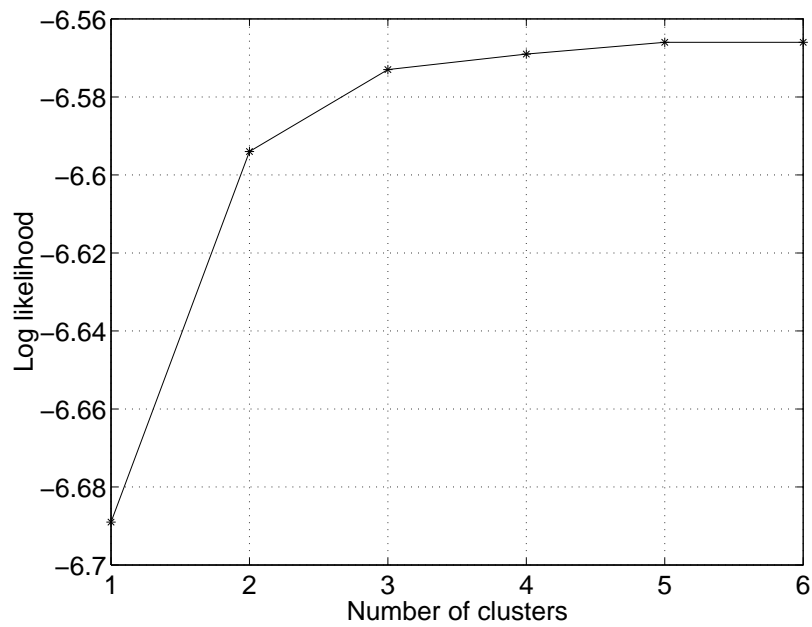


Figure 6: Cross-validated log-likelihood per sample as a function of the number of clusters, computed by randomly dividing the dataset into two equal partitions 20 times; see Smyth et al. (1999) for details.

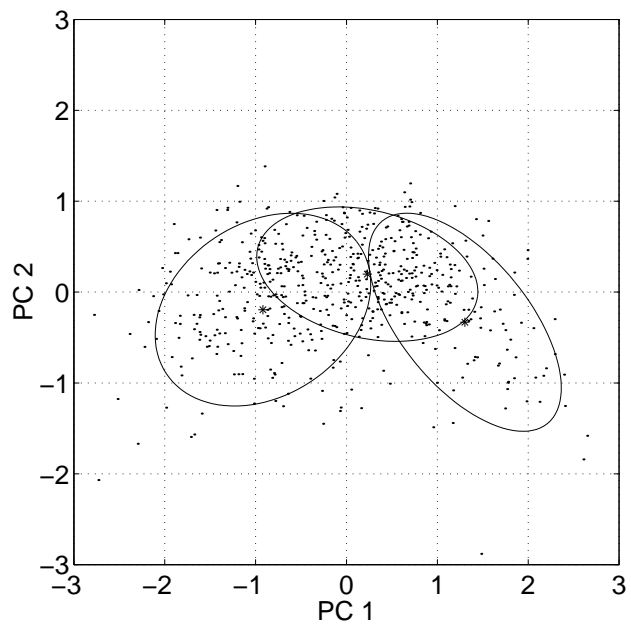


Figure 7: Mixture model estimates of regime centroids, denoted by the symbol *, and covariance ellipses, superimposed on the data scatter. Only every 50th data point has been plotted for clarity.

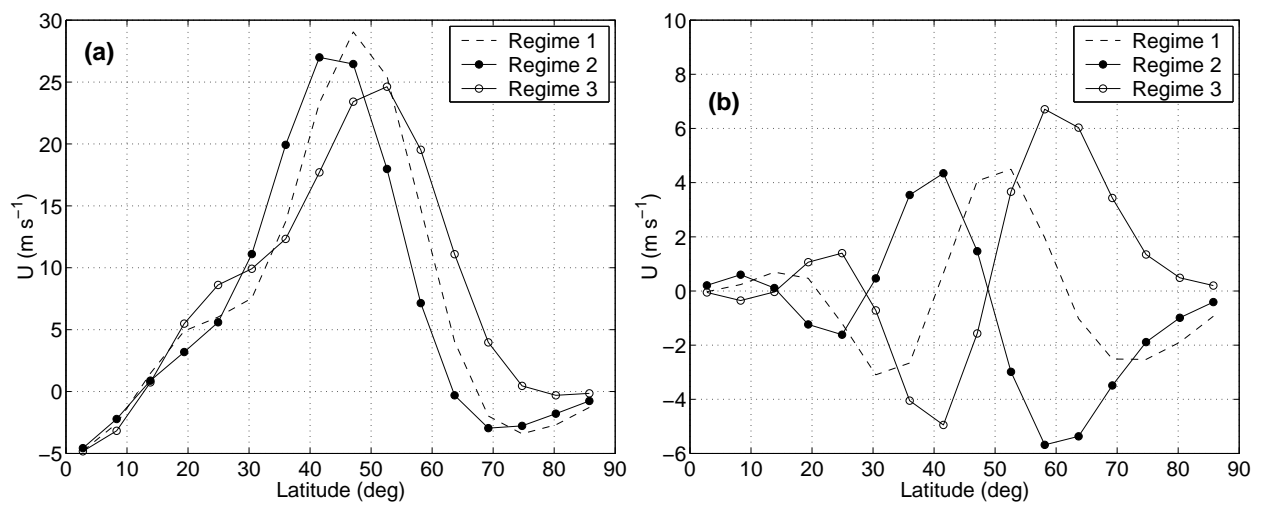


Figure 8: Composites of zonally and vertically averaged (a) total and (b) anomalous zonal-wind profile that belongs to the regime events.

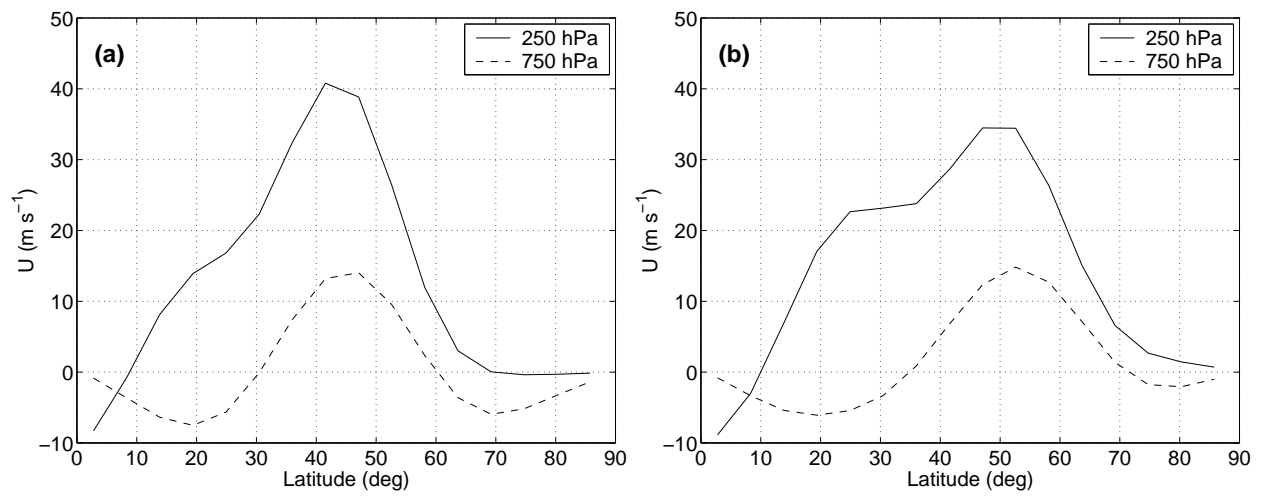


Figure 9: Composites of zonal mean wind at the two model levels for the (a) low- and (b) high-latitude regime events.

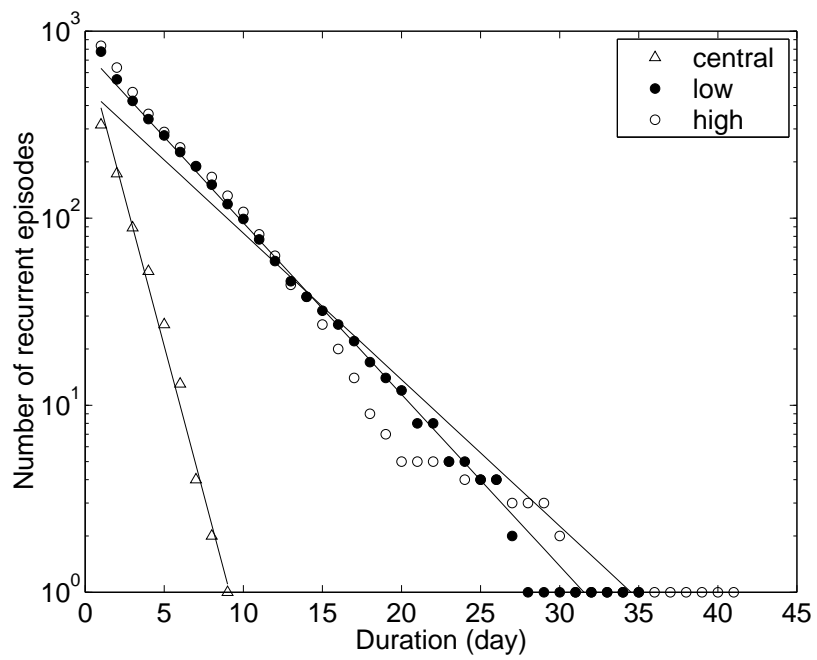


Figure 10: Persistence diagram of recurrent episodes.

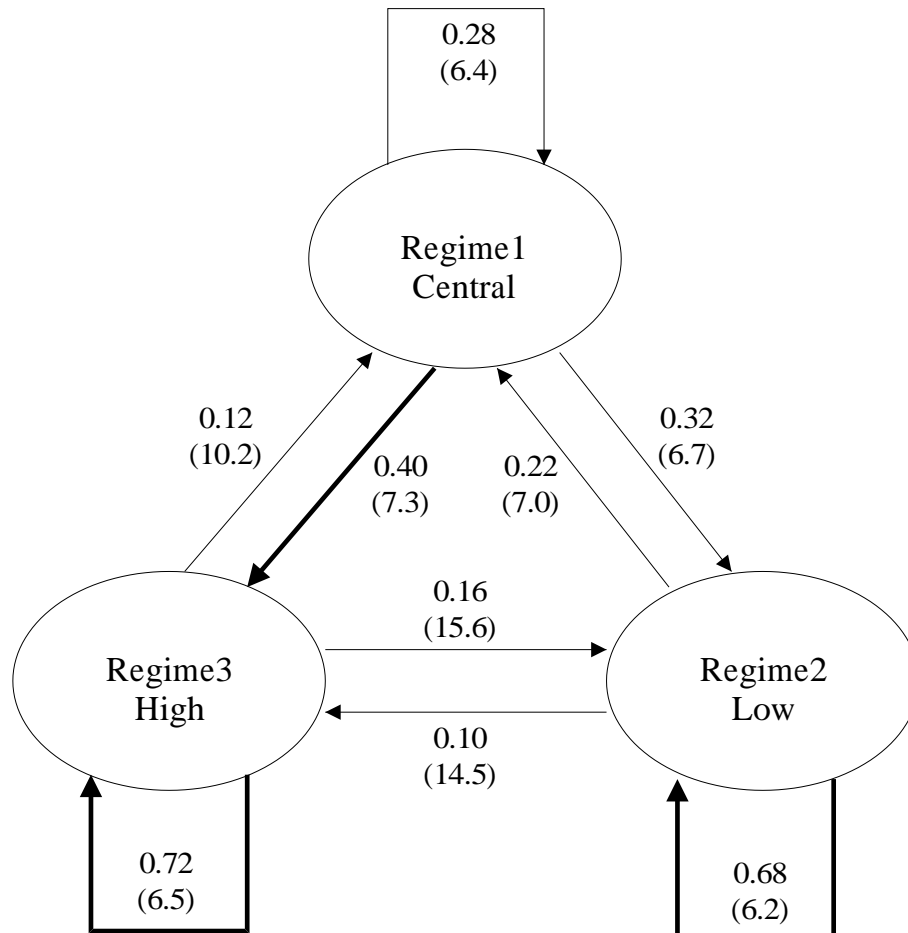


Figure 11: Markov chain of regime transitions. Numbers indicate transition probability and mean transition time (in parenthesis). Transitions that are statistically significant (Mo and Ghil 1988) at the 99% level are drawn as heavy arrows.

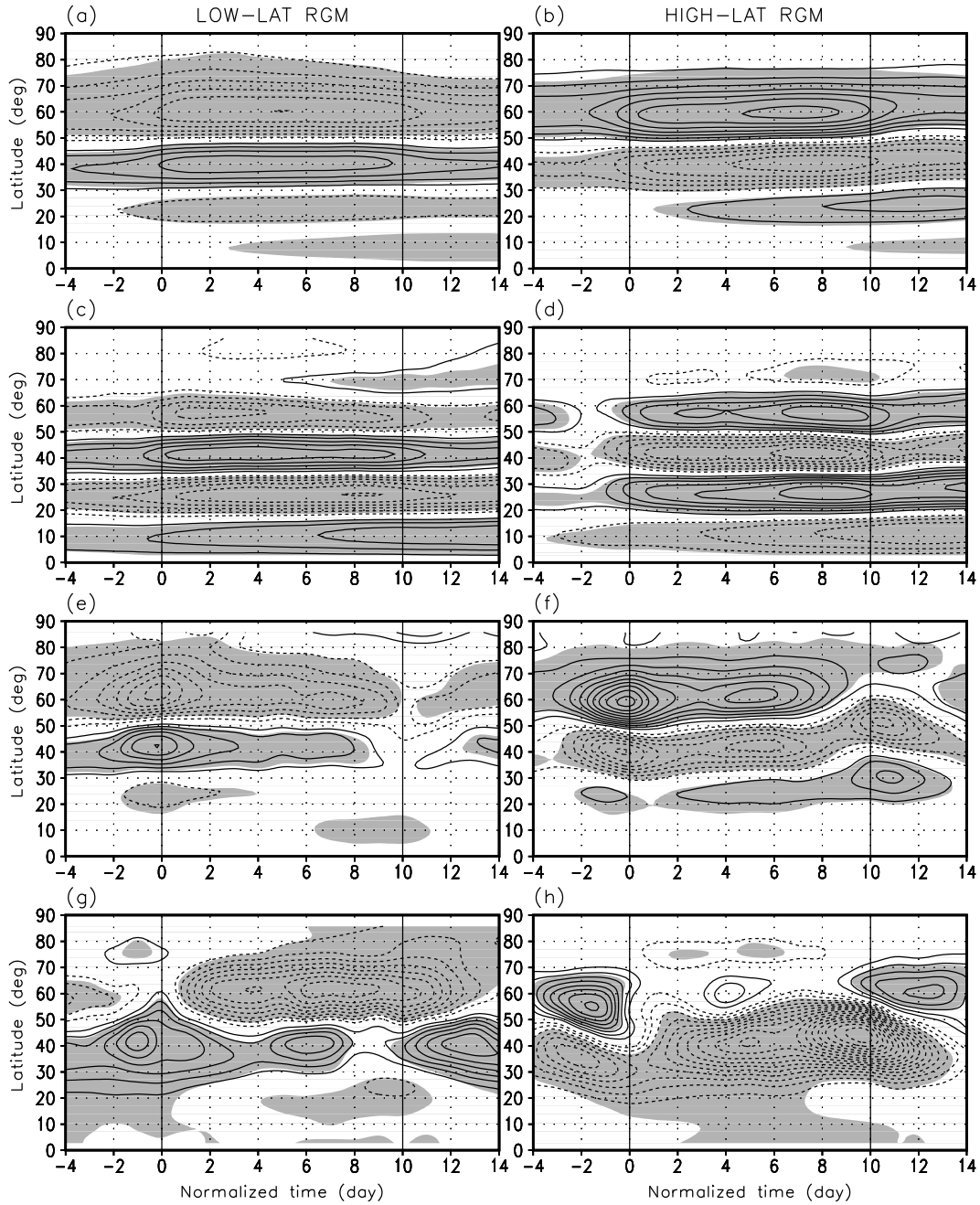


Figure 12: Composite anomalies with respect to standardized regime evolution: (a) and (b) vertically averaged zonal mean wind; (c) and (d) vertical wind shear; (e) and (f) vertically averaged eddy momentum flux convergence; and (g) and (h) low-level eddy heat flux. The left panels are for the low-latitude regime and the right panels for the high-latitude regime. Regime onset and break correspond to nondimensionalized time 0 and 10, respectively. The contour interval in (a) and (b) is 1.0 ms^{-1} , in (c) and (d) is 0.5 ms^{-1} , in (e) and (f) is $2.5 \times 10^{-6} \text{ ms}^{-2}$, and in (g) and (h) is 0.5 Kms^{-1} . Solid contours are positive, dashed ones are negative, and zero contour is omitted. Shaded areas are statistically significant at the 95% level (see text for details).

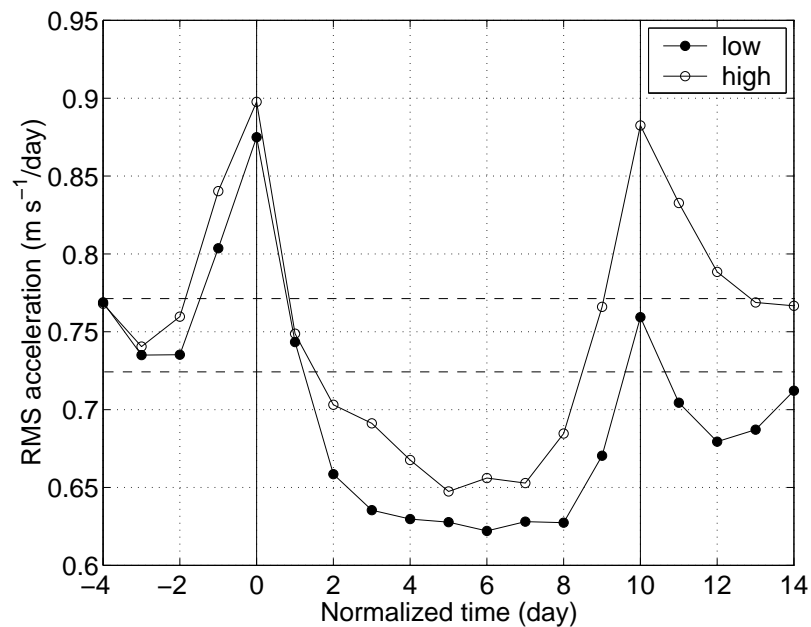


Figure 13: Composites of a root-mean-square (RMS) measure of acceleration of zonal mean wind, with respect to standardized regime evolution. This measure of acceleration is defined by the RMS difference between two meridional profiles, two days apart, of zonally and vertically averaged zonal wind, divided by the time elapsed. Onset and break correspond to the normalized epochs of 0 and 10 days, respectively. Dashed lines indicate a 95% confidence interval for the estimated climatological mean value of the RMS acceleration.

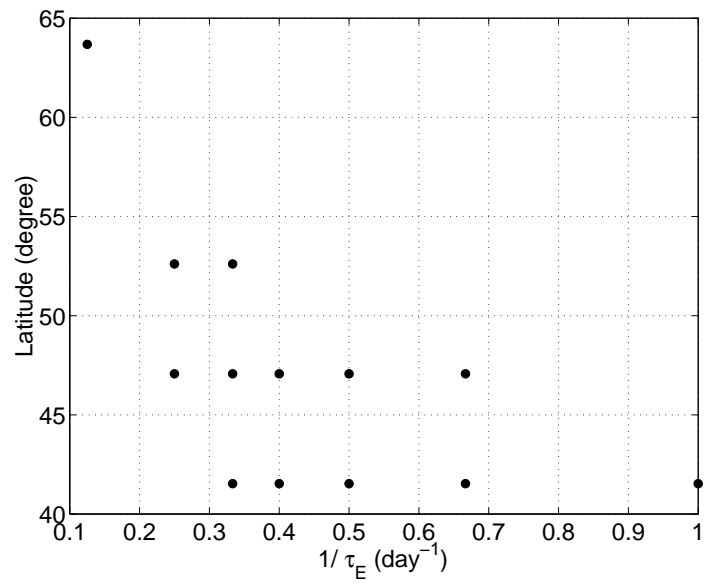


Figure 14: Dependence of the latitudinal position of the preferred regimes' zonal-jet maximum on bottom friction.

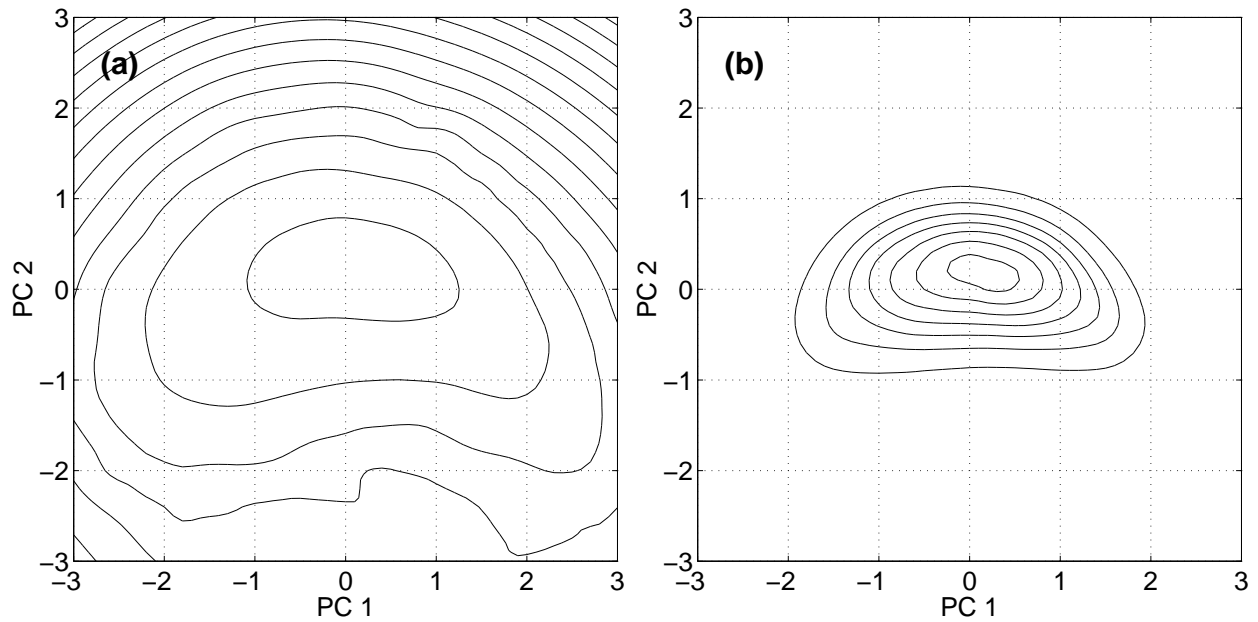


Figure A1: (a) Potential function used in Eq. (A1) to generate random time series. Contours are increasing from 3 (innermost one) in intervals of 3. (b) Asymptotic PDF of random time series of 200 000 samples generated from Eq. (A1) using the potential function in (a). Contours are increasing from 0.04 (outermost) in intervals of 0.04, as in Fig. 4a.